Nonlinear Dynamic Control Derivative Analysis for Aircraft with Application to Transonic Truss-Braced Wing

Nhan Nguyen*
NASA Ames Research Center, Moffett Field, CA 94035
Juntao Xiong†
KBR Wyle, Inc., Moffett Field, CA 94035

This paper presents the development of a nonlinear dynamic control derivative estimation method. A nonlinear aerodynamic model is developed to account for the effects of large control surface deflections on aircraft aerodynamic forces and moments. A series of unsteady RANS CFD simulations is performed to simulate the control surface oscillations at various reduced frequencies. The time-domain data are transformed into the frequency-domain data by a Fourier series analysis. Transfer functions of the dynamic control derivatives are then estimated by a frequency-domain regression. The method is applied to the Transonic Truss-Braced Wing (TTBW) to estimate the dynamic control derivatives for the elevator, aileron, and rudder.

I. Introduction

Vehicle stability and control is an area of study that deals with the design and analysis aspects of aircraft stability and control. Vehicle stability requires that an aircraft design be statically and dynamically stable and controllable in all three axes of the motion in roll, pitch, and yaw. Vehicle control is accomplished by aerodynamic control surfaces or other control effectors.

A stability and control analysis is usually required to determine a set of stability and control derivatives with respect to the aircraft state and control variables. The stability and control derivatives include both steady state derivatives such as C_{m_α},the pitching moment stability derivative with respect to the angle of attack, and $C_{m_{\delta_e}}$, the pitching moment control derivative with respect to the elevator deflection . Dynamic derivatives are the sensitivities evaluated by the partial derivatives with respect to the dynamic state variables of the aircraft such as the pitch rate q and control surface acceleration $\ddot{\delta}_e$. The dynamic stability derivatives with respect to the angular rates p, q, and r generally can be computed by some analytical techniques. On the other hand, dynamic derivatives with respect to the time derivatives of the aircraft state and control variables are more difficult to established. These derivatives account for the time delay in the aerodynamic response of the aircraft which can be important. The steady state and dynamic stability derivatives can be estimated experimentally by stability-and-control wind tunnel experiments or analytically by unsteady flow simulations.

The numerical estimation of dynamic stability and control derivatives is a current research topic. Recent work in this area can be found in many references.[1–3] Many of these technique do not adequately capture the various terms of the dynamic stability derivatives. More importantly, the effects of the frequency response on the dynamic stability derivatives is not well addressed especially for aircraft operating in transonic flight regime. Murman uses reduced-frequency approach to address the frequency response, but the approach lacks sufficient details to enable a systematic approach to determining the dynamic stability derivatives.[3] A frequency-domain dynamic stability estimation has recently been developed[4] and applied to the Mach 0.8 Transonic Truss-Braced Wing (TTBW) aircraft,[5] shown in Figure 1. Using unsteady RANS CFD simulation results, the time histories of the aerodynamic coefficients are transformed into the frequency domain by a Fourier series analysis as a function of the reduced frequency. A frequency-domain transfer function is designed to capture both the steady state and dynamic derivatives. The transfer function is formulated based on the Theodorsen's theory.[7] A frequency-domain regression analysis is then performed to estimate the

*Senior Research Scientist and Technical Group Lead of Advanced Control and Engineering Systems Group, Intelligent Systems Division, nhan.t.nguyen@nasa.gov
†Aerospace Engineer, Intelligent System Division, juntao.xiong@nasa.gov

transfer function. The proposed method can estimate those dynamic stability derivatives that are usually not captured in many analyses but do exist in the Theordorsen's theory such as $C_{m_{\dot{q}}}$ due to the apparent mass effect.

Figure 1. Boeing Mach 0.8 Transonic Truss-Braced Wing Aircraft Concept

This study continues the investigation of the stability and control estimation using high-fidelity CFD. In this study, we develop a frequency-domain estimation of the control derivatives for the TTBW taking into account significant nonlinearity in the aerodynamic response due to the large control surface deflections.[7] In our prior work, we have completed the estimation of the dynamic control derivatives for the elevator.[7] In this work, we present the results of the estimation of the dynamic control derivatives for the aileron and rudder.

II. Nonlinear Dynamic Control Derivative Estimation Method

Consider the harmonic motion of a control surface prescribed by

$$\tilde{\delta} = \delta_0 \sin k\tau \tag{1}$$

where $\tau = \frac{2V_\infty}{\bar{c}} t$ is the non-dimensional time and $k = \frac{\omega \bar{c}}{2V_\infty}$ is the reduced frequency.

In the previous work,[7] we presented a model of the unsteady aerodynamic coefficient as an n^{th}-degree polynomial of the deflection given by

$$\begin{aligned} \tilde{C}_L &= H_L(\bar{s}) \left(\sum_{j=1}^{n} \sigma_j \tilde{\delta}^j + \sum_{j=1}^{n} \mu_j \tilde{\delta}^{j-1} \frac{d\tilde{\delta}}{d\tau} \right) + d_1 \frac{d\tilde{\delta}}{d\tau} + d_2 \frac{d^2\tilde{\delta}}{d\tau^2} \\ &= H_L(\bar{s}) \sum_{j=1}^{3} (\sigma_j + \mu_j \bar{s}) \tilde{\delta}^j + \left(d_1 \bar{s} + d_2 \bar{s}^2 \right) \tilde{\delta} \end{aligned} \tag{2}$$

where $\bar{s} = \frac{s\bar{c}}{2V_\infty}$ is the non-dimensional Laplace variable. A 6^{th}-degree polynomial is sufficient to capture the unsteady aerodynamic coefficients. The unsteady aerodynamic coefficient is then expressed in term of the control derivatives as

$$\tilde{C}_L = \sum_{j=1}^{6} \tilde{C}_{L_{\tilde{\delta}^j}}(\bar{s}) \tilde{\delta}^j \tag{3}$$

where $C_{L_{\tilde{\delta}j}}(\bar{s})$ are the dynamic control derivatives. When $j=1$, the dynamic control derivatives are linear. The dynamic control derivatives are generally functions of the reduced frequency and are to be computed from the CFD simulation data. The Fourier series representation of the dynamic control derivatives is given by

$$\tilde{C}_{L_{\tilde{\delta}j}}(\bar{s}) = Q_j(k) + iS_j(k) \tag{4}$$

where $Q_j(k)$ and $S_j(k)$ are the real parts and imaginary parts of $\tilde{C}_{L_{\tilde{\delta}j}}(\bar{s})$. The imaginary part implies a differentiation since $i = \frac{\bar{s}}{k} = \frac{1}{k}\frac{d}{d\tau}$ which accounts for the phase shift.

Upon expansion and removing the constants in the even-power nonlinear terms $\tilde{\delta}^2$ and $\tilde{\delta}^4$, we have

$$\begin{aligned}
\tilde{C}_L = {} & [Q_1(k) + iS_1(k)]\,\delta_0 \sin k\tau + [Q_2(k) + iS_2(k)]\,\delta_0^2 \left(-\frac{1}{2}\cos 2k\tau\right) \\
& + [Q_3(k) + iS_3(k)]\,\delta_0^3 \left(-\frac{1}{4}\sin 3k\tau + \frac{3}{4}\sin k\tau\right) \\
& + [Q_4(k) + iS_4(k)]\,\delta_0^4 \left(\frac{1}{8}\cos 4k\tau - \frac{1}{2}\cos 2k\tau\right) \\
& + [Q_5(k) + iS_5(k)]\,\delta_0^5 \left(\frac{1}{16}\sin 5k\tau - \frac{5}{16}\sin 3k\tau + \frac{5}{8}\sin k\tau\right) \\
& + [Q_6(k) + iS_6(k)]\,\delta_0^6 \left(-\frac{1}{32}\cos 6k\tau + \frac{3}{16}\cos 4k\tau - \frac{15}{32}\cos 2k\tau\right)
\end{aligned} \tag{5}$$

We see that the odd-power nonlinear terms $\tilde{\delta}^3$ and $\tilde{\delta}^5$ contain first harmonic components which also contribute to the linear term $\tilde{\delta}$. The Fourier series coefficients $Q_j(k)$ and $S_j(k)$ are readily obtained from the Fourier series analysis as

$$Q_1(k) = \frac{k\int_0^{\frac{2N_p\pi}{k}} \tilde{C}_D(\sin k\tau + 3\sin 3k\tau + 5\sin 5k\tau)\,d\tau}{N_p\pi\delta_0} \tag{6}$$

$$S_1(k) = \frac{k\int_0^{\frac{2N_p\pi}{k}} \tilde{C}_D(\cos k\tau + 3\cos 3k\tau + 5\cos 5k\tau)\,d\tau}{N_p\pi\delta_0} \tag{7}$$

$$Q_2(k) = \frac{-2k\int_0^{\frac{2N_p\pi}{k}} \tilde{C}_D(\cos 2k\tau + 4\cos 4k\tau + 9\cos 6k\tau)\,d\tau}{N_p\pi\delta_0^2} \tag{8}$$

$$S_2(k) = \frac{2k\int_0^{\frac{2N_p\pi}{k}} \tilde{C}_D(\sin 2k\tau d\tau + 4\sin 4k\tau + 9\sin 6k\tau)\,d\tau}{N_p\pi\delta_0^2} \tag{9}$$

$$Q_3(k) = \frac{-4k\int_0^{\frac{2n\pi}{k}} \tilde{C}_D(\sin 3k\tau + 5\sin 5k\tau)\,d\tau}{N_p\pi\delta_0^3} \tag{10}$$

$$S_3(k) = \frac{-4k\int_0^{\frac{2N_p\pi}{k}} \tilde{C}_D(\cos 3k\tau + 5\cos 5k\tau)\,d\tau}{N_p\pi\delta_0^3} \tag{11}$$

$$Q_4(k) = \frac{8k\int_0^{\frac{2N_p\pi}{k}} \tilde{C}_D(\cos 4k\tau + 6\cos 6k\tau)\,d\tau}{N_p\pi\delta_0^4} \tag{12}$$

$$S_4(k) = \frac{-8k\int_0^{\frac{2N_p\pi}{k}} \tilde{C}_D(\sin 4k\tau + 6\sin 6k\tau)\,d\tau}{N_p\pi\delta_0^4} \tag{13}$$

$$Q_5(k) = \frac{16k\int_0^{\frac{2N_p\pi}{k}} \tilde{C}_D \sin 5k\tau d\tau}{N_p\pi\delta_0^5} \tag{14}$$

$$S_5(k) = \frac{16k\int_0^{\frac{2N_p\pi}{k}} \tilde{C}_D \cos 5k\tau d\tau}{N_p \pi \delta_0^5} \tag{15}$$

$$Q_6(k) = \frac{-32k\int_0^{\frac{2N_p\pi}{k}} \tilde{C}_D \cos 6k\tau d\tau}{N_p \pi \delta_0^6} \tag{16}$$

$$S_6(k) = \frac{32k\int_0^{\frac{2N_p\pi}{k}} \tilde{C}_D \sin 6k\tau d\tau}{N_p \pi \delta_0^6} \tag{17}$$

From the expressions for the unsteady aerodynamic coefficient, the dynamic control derivatives are expressed as

$$\tilde{C}_{L_{\tilde{\delta}j}}(\bar{s}) = \begin{cases} H_L(\bar{s})(\sigma_j + \mu_j \bar{s}) + d_1 \bar{s} + d_2 \bar{s}^2 & j = 1 \\ H_L(\bar{s})(\sigma_j + \mu_j \bar{s}) & j \neq 1 \end{cases} \tag{18}$$

The unsteady aerodynamic transfer function $H_L(\bar{s})$ has a form

$$H_L(\bar{s}) = 1 + \frac{\sum_{j=1}^{m} a_j \bar{s}^j}{\bar{s}^n + \sum_{j=0}^{n-1} b_j \bar{s}^j} \tag{19}$$

where $m \leq n$. Thus, $H_L(\bar{s})$ and the coefficients d_1, d_2, σ_j and μ_j can be estimated by a frequency-domain regression which has been developed in the previous work.[7] The frequency-domain regression fits the unsteady aerodynamic model over the frequency response data obtained by the Fourier series coefficients $Q_j(k)$ and $S_j(k)$. From the frequency-domain regression results, the linear dynamic control derivatives are obtained as

$$C_{L_\delta}(\bar{s}) = H_L(\bar{s})\sigma_1 \tag{20}$$

$$C_{L_{\dot{\delta}}}(\bar{s}) = H_L(\bar{s})\mu_1 + d_1 \tag{21}$$

$$C_{L_{\ddot{\delta}}} = d_2 \tag{22}$$

The nonlinear dynamic control derivatives are obtained as

$$C_{L_{\delta j}}(\bar{s}) = H_L(\bar{s})\sigma_j \tag{23}$$

$$C_{L_{\dot{\delta} j}}(\bar{s}) = H_L(\bar{s})\mu_j \tag{24}$$

for $j \neq 1$. Note that $C_{L_{\dot{\delta}j}}(\bar{s})$ should be interpreted as $\frac{\partial C_L}{\partial\left(\frac{d(\delta j)}{dt}\right)}$.

III. Determination of Dynamic Control Derivatives of Transonic Truss-Braced Wing

The dynamic control derivative estimation method is applied to the Mach 0.8 TTBW. Figure 2 illustrates control surface layout for the Mach 0.8 TTBW.[8] A series of unsteady RANS CFD simulations of the control surface oscillations of the elevator, outboard all-speed aileron, and rudder of the Mach 0.8 TTBW is conducted in FUN3D.[9] The FUN3D tetrahedral prism mesh has about 96 million nodes. The Roe's flux-difference splitting scheme and the Spalart-Allmaras turbulence model are used in the simulations. An optimized second-order backward finite-difference scheme is used in the time integration. The aircraft is trimmed with the horizontal tail incidence of -0.75° at the design lift coefficient $C_L = 0.695$ and an altitude of 46,716 ft corresponding to the mid-cruise gross weight of 130,486 lbs for the Mach 0.8 TTBW.

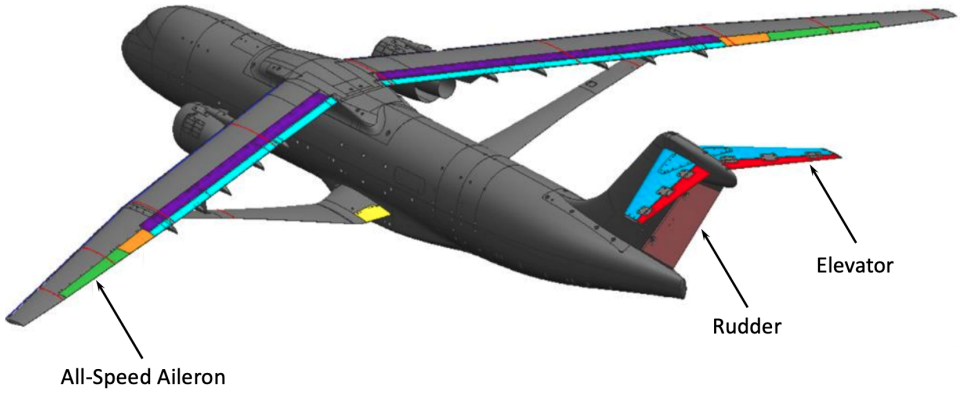

Figure 2. Control Surface Layout of Mach 0.8 Transonic Truss Braced-Wing

A. Elevator Dynamic Control Derivative Estimation

The elevator control surface oscillations are simulated with four different amplitudes of 0.1°, 1°, and 20°, each at three reduced frequencies $k = 0.02$, 0.1, and 0.2. The left and right elevator control surfaces are modeled as a single unit deflected in a symmetric motion for pitch control. Frequency response data are generated by curve fitting for the frequency-domain regression.

Figure 3(a) shows the pressure contour plots for various elevator deflections. The flow over the horizontal tail is seen to be entirely subsonic for small elevator deflections up to about 1° or less. Shock-induced boundary layer separation at the hinge line is observed when the elevator deflection is about 10°. Figure 3(b) shows the pressure distribution on a horizontal tail section with the elevator deflected at 20°. The pressure distribution indicates a flow separation region on the entire elevator control surface.

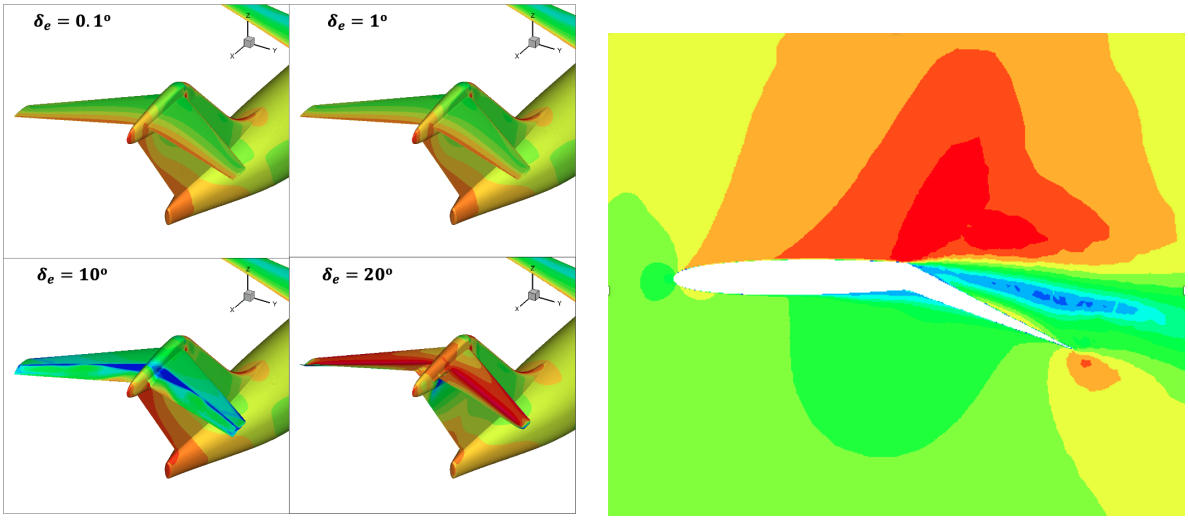

(a) (b)

Figure 3. Instantaneous Pressure Contour Due to Elevator Deflection

The plots of the unsteady lift, pitching moment, and drag coefficients versus the elevator deflection are shown in Figs. 4(a), (b), and (c), respectively. The lift and pitching moment coefficients are modeled with a polynomial degree $n = 3$ and the drag coefficient is modeled with a polynomial degree $n = 6$. The plots of the Fourier series of these coefficients are also shown. The Fourier series reconstruction agrees well with the simulation data. The data shows significant nonlinearity. A linear response would have appeared as an elliptical curve for the lift and pitching moment coefficients.

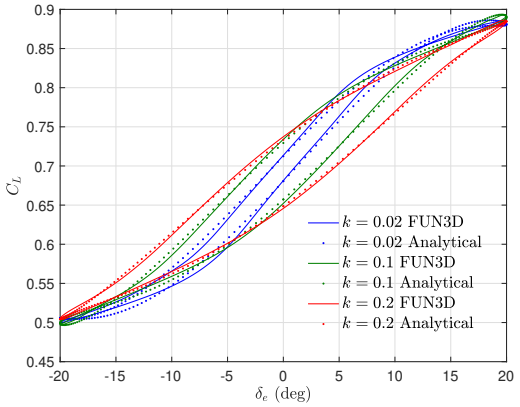

(a) $\tilde{C}_L$ vs. $\tilde{\delta}_e$

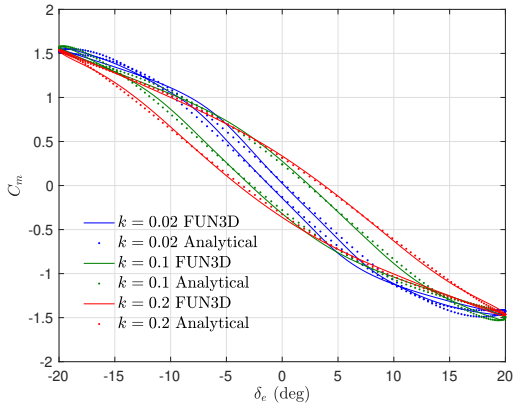

(b) $\tilde{C}_m$ vs. $\tilde{\delta}_e$

(a) $\tilde{C}_L$ vs. $\tilde{\delta}_e$

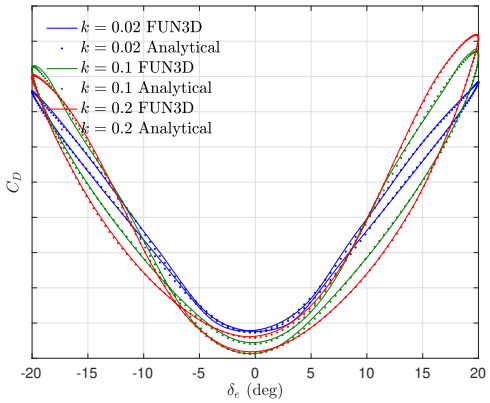

(c) $\tilde{C}_D$ vs. $\tilde{\delta}_e$

Figure 4. Lift, Pitching Moment, and Drag Coefficients vs. Elevator Deflection

	$\tilde{C}_{L_{\tilde{\delta}_e}}$	$\tilde{C}_{m_{\tilde{\delta}_e}}$	$\tilde{C}_{D_{\tilde{\delta}_e}}$
a_1	-0.04044	-0.05383	-0.03018
b_0	0.006508	0.01311	0.03769
b_1	0.2316	0.2651	0.3883
c_0	0.9149	-6.994	0.005826
c_1	13.95	-68.10	0.04143
d_1	-13.63	67.40	-0.02850
d_2	-0.8283	2.527	-0.01744

Table 1. Regression Coefficients of Linear Dynamic Control Derivatives of Lift, Pitching Moment, and Drag Coefficients for Elevator

The linear dynamic control derivatives are of the form

$$\tilde{C}_{L,m,D_{\tilde{\delta}_e}} = \left(1 + \frac{a_1\bar{s}}{\bar{s}^2 + b_1\bar{s} + b_0}\right)(c_0 + c_1\bar{s}) + d_1\bar{s} + d_2\bar{s}_2 \tag{25}$$

where the regression coefficients are given in Table 1. The steady-state dynamic linear control derivatives at zero

frequency are given by $C_{L,m,D_{\delta_e}} = c_0$, $C_{L,m,D_{\dot{\delta}_e}} = c_1 + d_1$, and $C_{L,m,D_{\ddot{\delta}_e}} = d_2$. The plots of the frequency-domain regression of the dynamic linear control derivatives for the elevator are shown in Fig. 5.

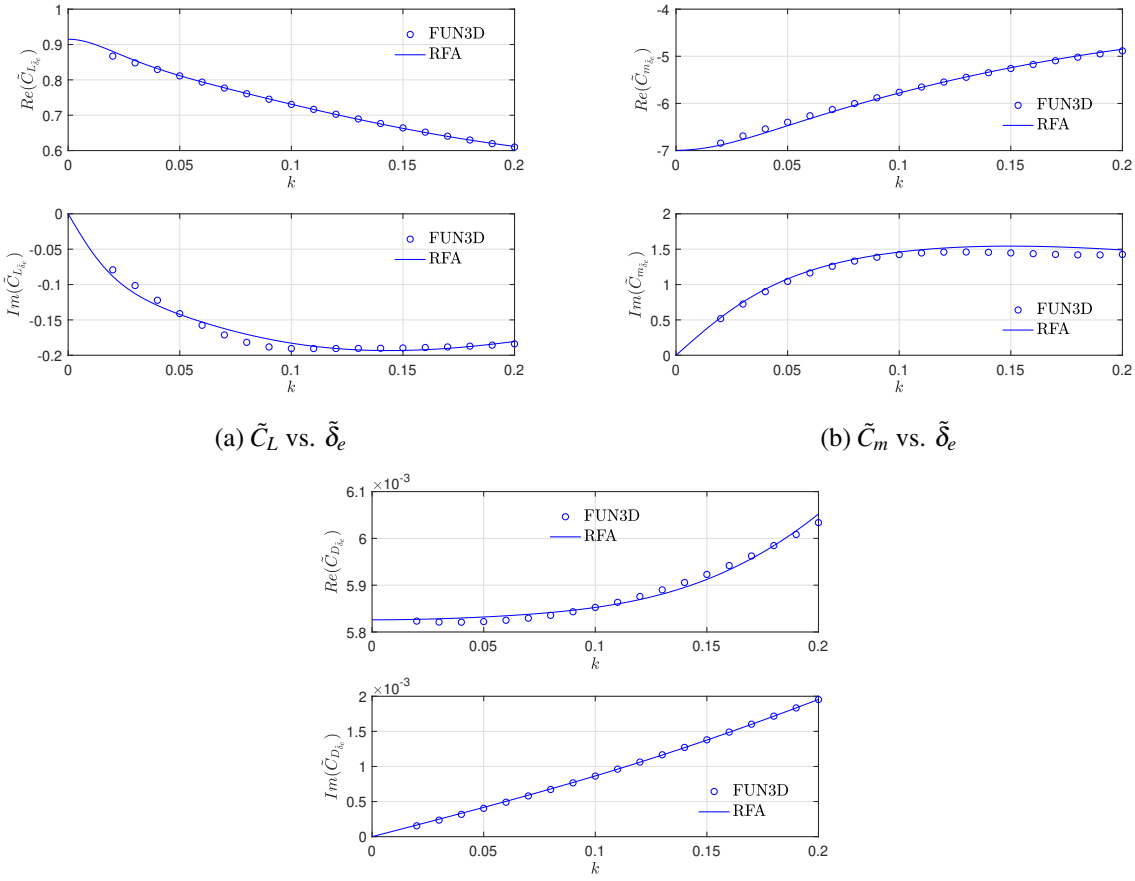

(a) $\tilde{C}_L$ vs. $\tilde{\delta}_e$

(b) $\tilde{C}_m$ vs. $\tilde{\delta}_e$

(c) $\tilde{C}_D$ vs. $\tilde{\delta}_e$

Figure 5. Frequency-Domain Regression of Linear Dynamic Control Derivatives of Lift, Pitching Moment, and Drag Coefficients for Elevator

The nonlinear dynamic control derivatives are of the form

$$\tilde{C}_{L,m,D_{\delta_e^j}} = \left(1 + \frac{a_4\bar{s}^4 + a_3\bar{s}^3 + a_2\bar{s}^2 + a_1\bar{s}}{\bar{s}^4 + b_3\bar{s}^3 + b_2\bar{s}^2 + b_1\bar{s} + b_0}\right)(c_0 + c_1\bar{s}) \tag{26}$$

where the regression coefficients are given in Table 2. The steady-state nonlinear dynamic control derivatives at zero frequency are given by $C_{L,m,D_{\delta_e^j}} = c_0$ and $C_{L,m,D_{\dot{\delta}_e^j}} = c_1$. The 2^{nd}-order nonlinear dynamic control derivatives of the lift and pitching moment coefficients and the 3^{rd}- and 5^{th}-order nonlinear dynamic control derivatives of the drag coefficient are generally small and therefore can be neglected. The plots of the frequency-domain regression of the nonlinear dynamic control derivatives for the elevator are shown in Figure 6.

	$\tilde{C}_{L_{\tilde{\delta}_e^3}}$	$\tilde{C}_{m_{\tilde{\delta}_e^3}}$	$\tilde{C}_{D_{\tilde{\delta}_e^2}}$	$\tilde{C}_{D_{\tilde{\delta}_e^4}}$	$\tilde{C}_{D_{\tilde{\delta}_e^6}}$
a_1	−0.006440	−0.009464	0.1504	−0.02170	−0.02099
a_2	−0.07857	−0.09893	1.878	−0.2018	−0.1826
a_3	−0.4160	−0.4575	8.570	−0.7681	−0.7365
a_4	−0.2472	−0.2384	27.18	−0.1755	0.2651
b_0	0.0007880	0.001171	0.09245	0.001500	0.001276
b_1	0.01888	0.02535	0.6708	0.03049	0.02706
b_2	0.1693	0.2056	1.825	0.2324	0.2148
b_3	0.6726	0.7407	2.206	0.7873	0.7573
c_0	−2.840	22.68	0.5898	−4.283	14.62
c_1	7.053	−50.76	−1.857	−42.75	185.4

Table 2. Coefficients of Nonlinear Control Derivatives of Lift, Pitching Moment, and Drag Coefficient for Elevator

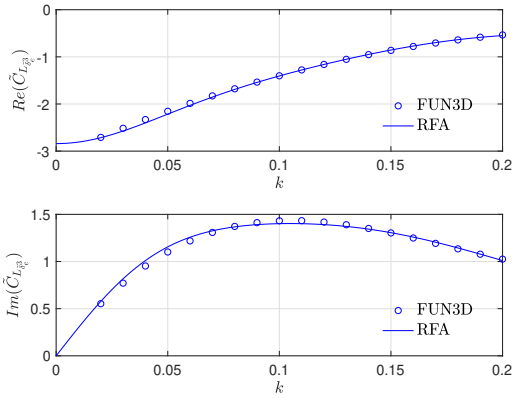

(a) $\tilde{C}_{L_{\tilde{\delta}_a^3}}$ vs. $\tilde{\delta}_e$

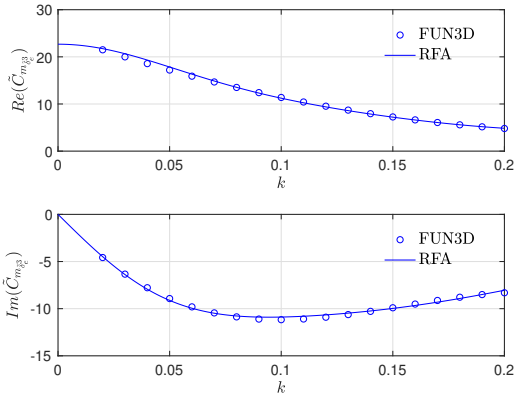

(b) $\tilde{C}_{m_{\tilde{\delta}_e^3}}$ vs. $\tilde{\delta}_e$

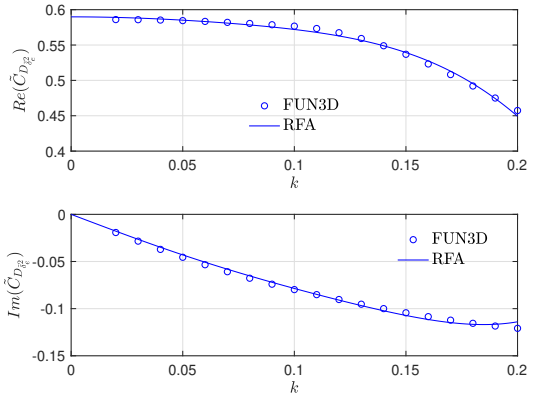

(c) $\tilde{C}_{D_{\tilde{\delta}_e^2}}$ vs. $\tilde{\delta}_e$

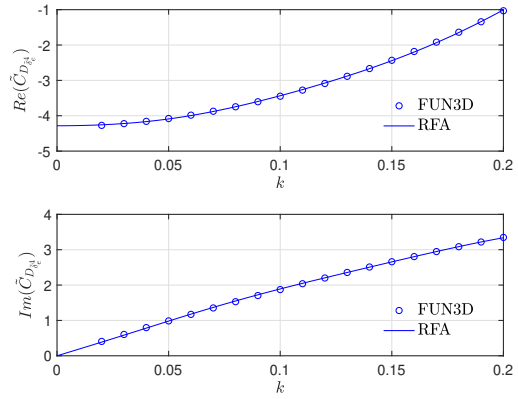

(d) $\tilde{C}_{D_{\tilde{\delta}_e^4}}$ vs. $\tilde{\delta}_e$

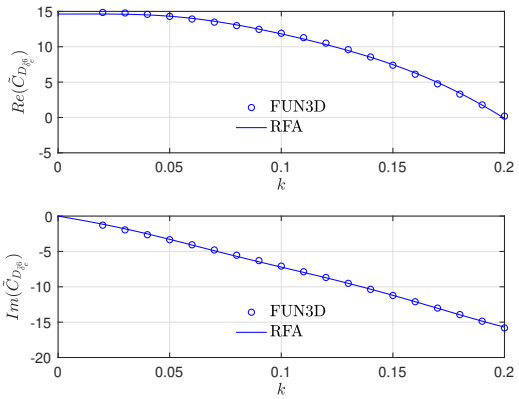

(e) $\tilde{C}_{D_{\tilde{\delta}_e}}$ vs. $\tilde{\delta}_e$

Figure 6. Frequency-Domain Regression of Nonlinear Dynamic Control Derivatives of Lift, Pitching Moment, and Drag Coefficients for Elevator

B. Aileron Dynamic Control Derivative Estimation

The aileron control surface oscillations are simulated with four different amplitudes of 0.1°, 1°, and 20°, each at three reduced frequencies $k = 0.02$, 0.1, and 0.2. The left and right aileron control surfaces are modeled as a single unit deflected in an anti-symmetric motion for roll control. Figure 7(a) shows the instantaneous pressure contour of the flow over the right wing with the right aileron deflected at 20°. Figure 7(b) shows a 2D pressure contour illustrated on a generic supercritical airfoil indicating a shock-induced flow separation at the hinge line.

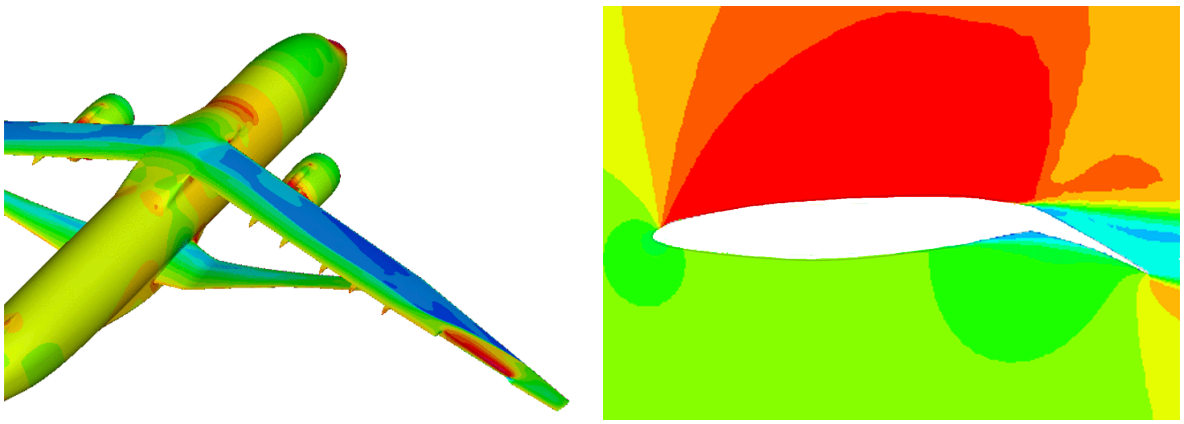

(a) (b)

Figure 7. Instantaneous Pressure Contour Due to Right Aileron Deflection at 20°

The plots of the unsteady side force, rolling moment, and yawing moment coefficients versus the aileron control surface deflection for an amplitude of 20° are shown in Figures 8(a), (b), and (c), respectively. The plots of the Fourier series of these aerodynamic coefficients are also shown. The Fourier series reconstruction using a polynomial degree $n = 5$ agrees well with the simulation data. The data shows significant nonlinearity in the side force and yawing moment coefficients.

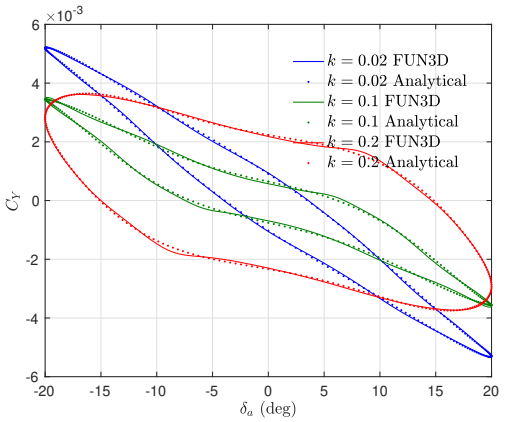

(a) $\tilde{C}_Y$ vs. $\tilde{\delta}_a$

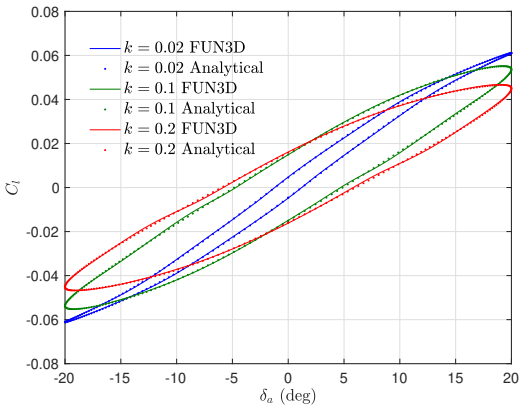

(b) $\tilde{C}_l$ vs. $\tilde{\delta}_a$

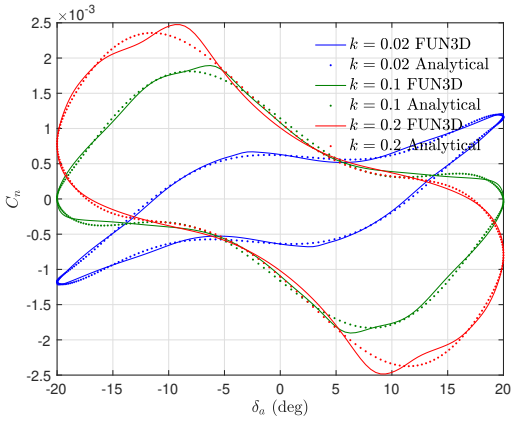

(c) $\tilde{C}_n$ vs. $\tilde{\delta}_a$

Figure 8. Side Force, Rolling Moment, and Yawing Moment Coefficients vs. Aileron Deflection

	$\tilde{C}_{Y_{\tilde{\delta}_e}}$	$\tilde{C}_{l_{\tilde{\delta}_e}}$	$\tilde{C}_{n_{\tilde{\delta}_e}}$
a_1	0.2050	−0.02344	−2.191
b_0	0.03764	0.006043	0.01887
b_1	0.3880	0.1555	0.2915
c_0	−0.005668	0.2178	0.0008567
c_1	−0.05710	2.860	−0.005013
d_1	0.1104	−2.993	−0.03883
d_2	−0.1315	0.3775	0.1483

Table 3. Regression Coefficients of Dynamic Linear Control Derivatives of Side Force, Rolling Moment, and Yawing Moment Coefficient for Aileron

The regression coefficients of the dynamic linear control derivatives of the side force, rolling moment, and yawing moment coefficients obtained from the frequency-domain regression using the data for the 20° aileron deflection amplitude are shown in Table 3. The linear dynamic control derivatives are of the same form as Eq. (25). The plots of the frequency-domain regression of the linear dynamic control derivatives for the aileron are shown in Figure 9.

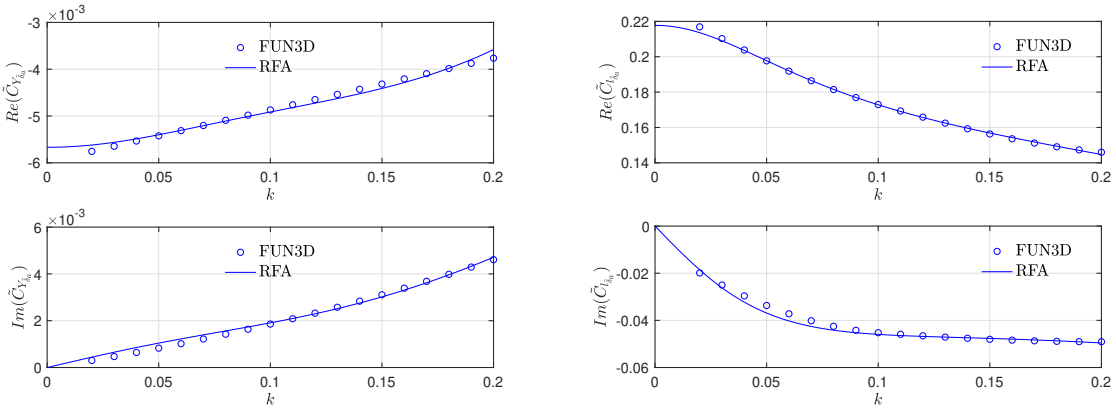

(a) $\tilde{C}_{Y_{\tilde{\delta}_a}}$ vs. $\tilde{\delta}_a$

(b) $\tilde{C}_{l_{\tilde{\delta}_a}}$ vs. $\tilde{\delta}_a$

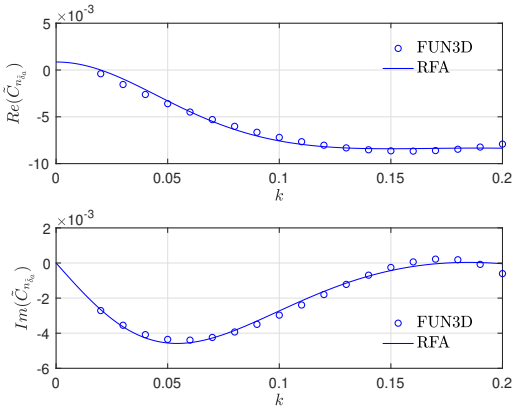

(c) $\tilde{C}_{n_{\tilde{\delta}_a}}$ vs. $\tilde{\delta}_a$

Figure 9. Frequency-Domain Regression of Linear Dynamic Control Derivatives of Side Force, Rolling Moment, and Yawing Moment Coefficients for Aileron

	$\tilde{C}_{Y_{\tilde{\delta}_a^3}}$	$\tilde{C}_{Y_{\tilde{\delta}_a^5}}$	$\tilde{C}_{l_{\tilde{\delta}_a^3}}$	$\tilde{C}_{l_{\tilde{\delta}_a^5}}$	$\tilde{C}_{n_{\tilde{\delta}_a^3}}$	$\tilde{C}_{n_{\tilde{\delta}_a^5}}$
a_1	0.03826	0.02076	0.01027	−0.3241	−0.02281	−0.01761
a_2	0.1893	0.1243	0.1456	15.27	−0.2049	−0.1865
a_3	0.5528	0.3627	0.8330	76.04	−0.8162	−0.7657
a_4	−1.460	1.222	1.405	419.2	−0.7097	−0.9339
b_0	0.001155	0.001373	0.001297	0.6837	0.001479	0.001072
b_1	0.02515	0.02853	0.02735	3.021	0.03018	0.02374
b_2	0.2048	0.2224	0.2162	4.990	0.2308	0.1969
b_3	0.7397	0.7701	0.7593	3.653	0.7846	0.7252
c_0	−0.02952	0.1918	−0.1383	0.4632	0.06315	−0.2716
c_1	0.06319	−0.8583	0.3488	9.075	1.729	−6.868

Table 4. Regression Coefficients of Nonlinear Control Derivatives of Side Force, Rolling Moment, and Yawing Moment Coefficients for Aileron

The regression coefficients of the nonlinear dynamic control derivatives of the side force, rolling moment, and yawing moment coefficients are shown in Table 4. The nonlinear dynamic control derivatives are of the same form as Eq. (26). The even-power nonlinear dynamic control derivatives are generally small and therefore negligible. The

plots of the frequency-domain regression of the nonlinear dynamic control derivatives for the aileron are shown in Fig. 10.

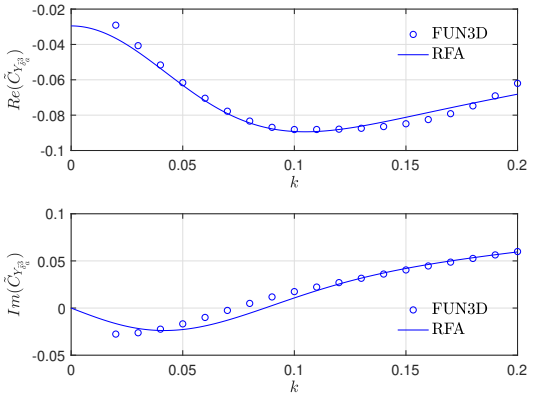

(a) $\tilde{C}_{Y_{\tilde{\delta}_a^3}}$ vs. $\tilde{\delta}_a$

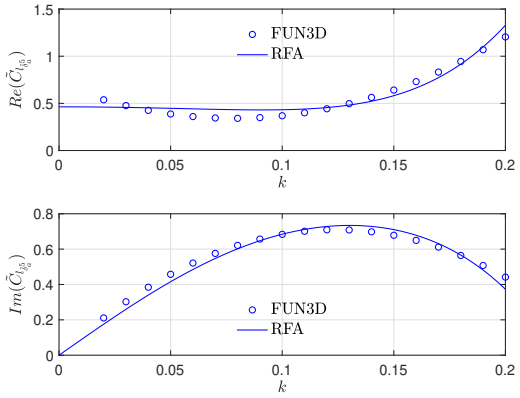

(b) $\tilde{C}_{Y_{\tilde{\delta}^5}}$ vs. $\tilde{\delta}_a$

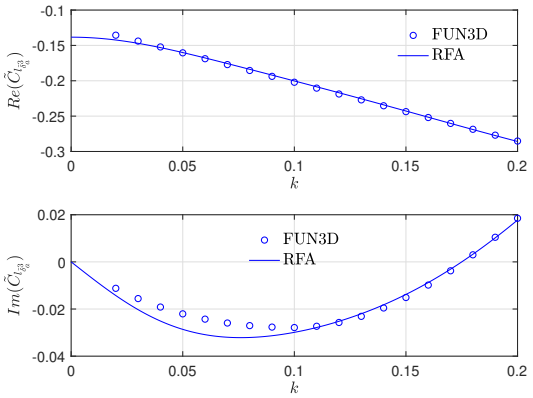

(a) $\tilde{C}_{l_{\tilde{\delta}_a^3}}$ vs. $\tilde{\delta}_a$

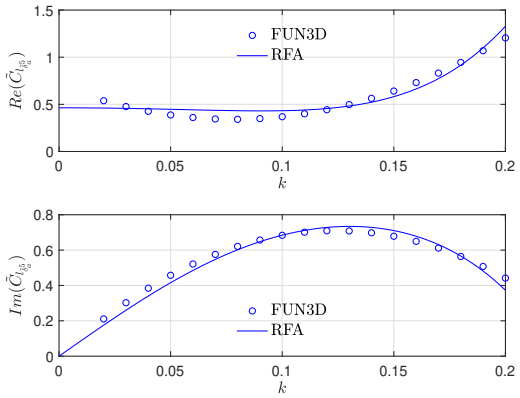

(a) $\tilde{C}_{l_{\tilde{\delta}_a^5}}$ vs. $\tilde{\delta}_a$

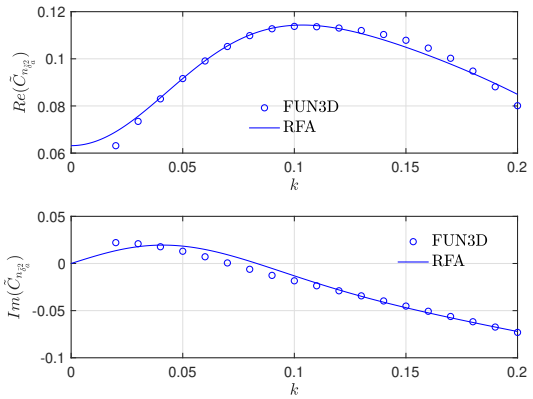

(a) $\tilde{C}_{n_{\tilde{\delta}_a^3}}$ vs. $\tilde{\delta}_a$

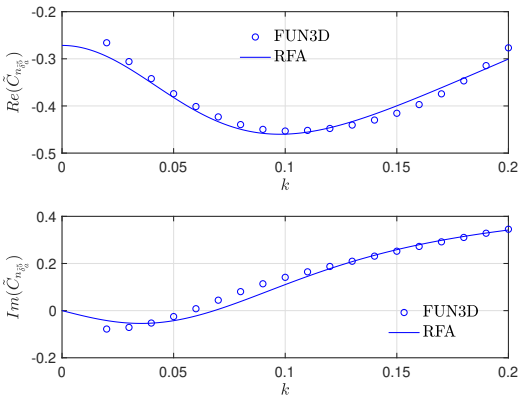

(a) $\tilde{C}_{n_{\tilde{\delta}_a^5}}$ vs. $\tilde{\delta}_a$

Figure 10. Frequency-Domain Regression of Nonlinear Dynamic Control Derivatives of Side Force, Rolling Moment, and Yawing Moment Coefficients for Aileron

C. Rudder Dynamic Control Derivative Estimation

The rudder control surface oscillations are simulated with four different amplitudes of 0.1°, 1°, and 10°, each at three reduced frequencies $k = 0.02$, 0.1, and 0.2. The rudder control surface is modeled using a blended mesh for the gap area. Figure 11(a) shows the instantaneous pressure contour with the rudder deflected at 10°. Figure 11(b) shows the pressure distribution on a vertical tail section which indicates a small shock at the hinge line, but the flow is predominantly attached.

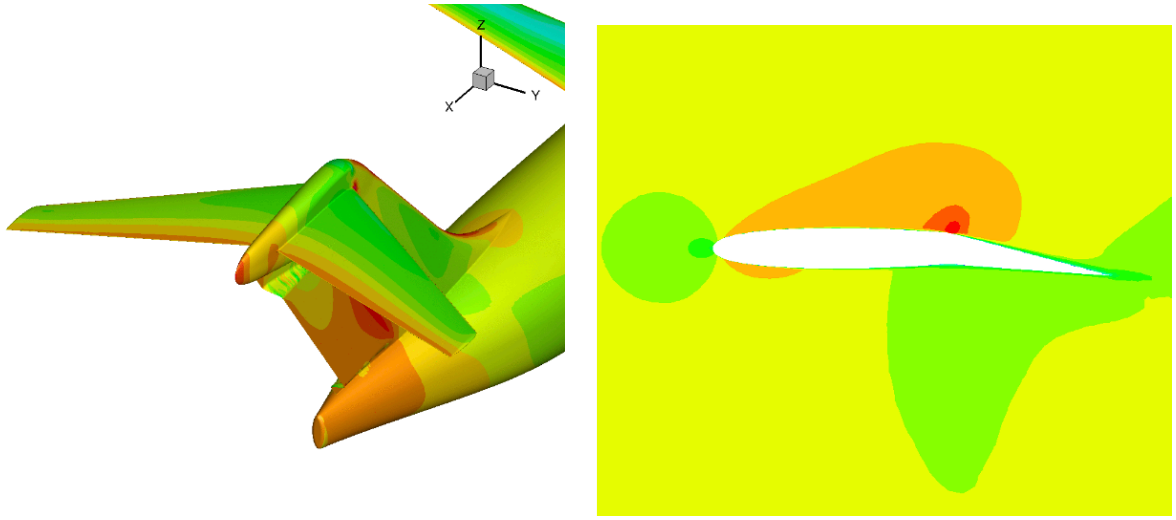

(a) (b)

Figure 11. Pressure Distribution with Rudder Deflection at 10°

The plots of the unsteady side force, rolling moment, and yawing moment coefficients versus the rudder deflection for an amplitude of 10° are shown in Figures 12(a), (b), and (c), respectively. The Fourier series reconstruction using a single harmonic agrees well with the data. This indicates that the side force, rolling moment, and yawing moment coefficients are generally linear with the rudder deflection up to 10°.

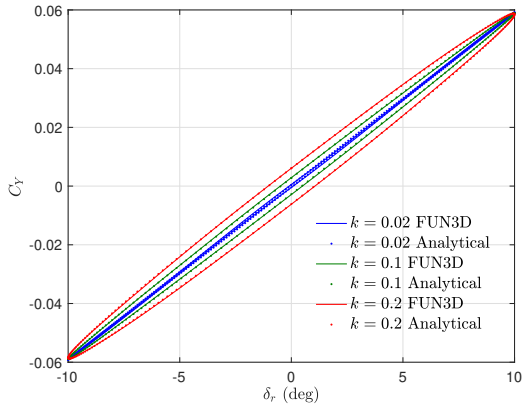

(a) $\tilde{C}_Y$ vs. $\tilde{\delta}_r$

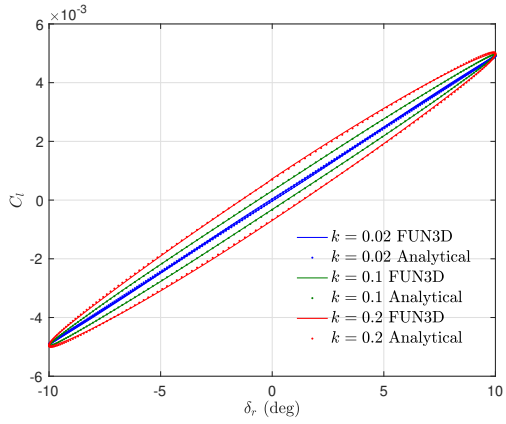

(b) $\tilde{C}_l$ vs. $\tilde{\delta}_r$

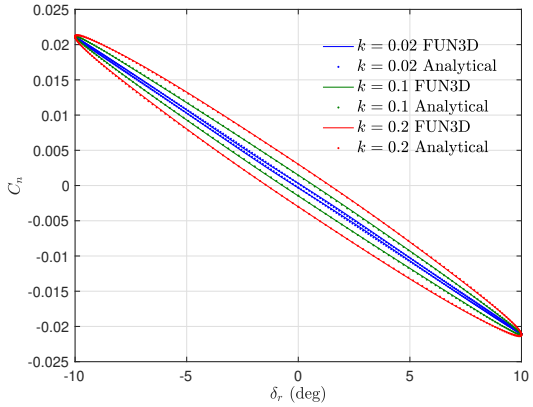

(c) $\tilde{C}_n$ vs. $\tilde{\delta}_r$

Figure 12. Side Force, Rolling Moment, and Yawing Moment Coefficients vs. Rudder Deflection

The regression coefficients of the linear dynamic control derivatives of the side force, rolling moment, and yawing moment coefficients obtained from the frequency-domain regression using the data for the 10° rudder deflection are shown in Table 5. The linear dynamic control derivatives are of the same form as Eq. (25). The nonlinear dynamic control derivatives for the rudder at a deflection up to 10° are generally small and therefore negligible. The plots of the frequency-domain regression of the linear dynamic control derivatives for the rudder are shown in Figure 13.

	$\tilde{C}_{Y_{\tilde{\delta}_r}}$	$\tilde{C}_{l_{\tilde{\delta}_r}}$	$\tilde{C}_{n_{\tilde{\delta}_r}}$
a_1	-0.006950	0	-0.009105
b_0	0.03823	0	0.03774
b_1	0.3911	0	0.3887
c_0	0.3390	0.02839	-0.1207
c_1	1.915	0	-1.249
d_1	-1.707	0	1.133
d_2	-0.06533	0	0.08951

Table 5. Regression Coefficients of Linear Dynamic Control Derivatives of Side Force, Rolling Moment, and Yawing Moment Coefficients for Rudder

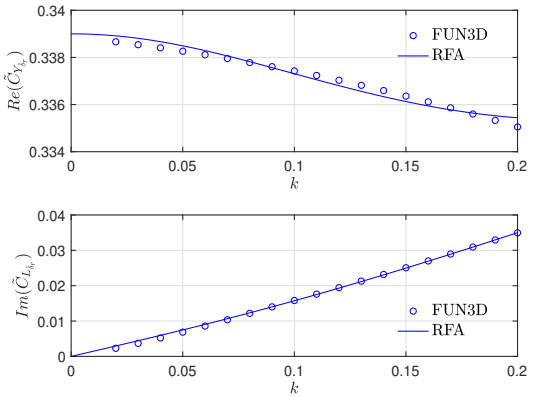

(a) $\tilde{C}_{Y_{\tilde{\delta}_r}}$ vs. $\tilde{\delta}_r$

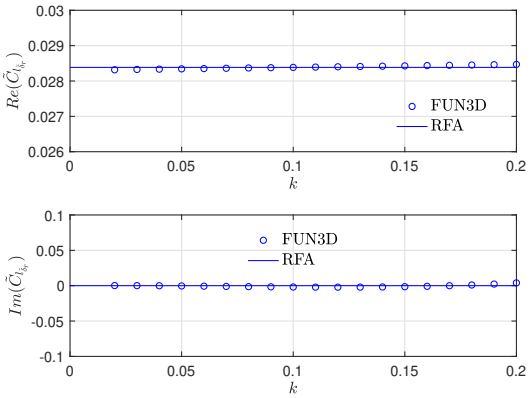

(b) $\tilde{C}_{l_{\tilde{\delta}_r}}$ vs. $\tilde{\delta}_r$

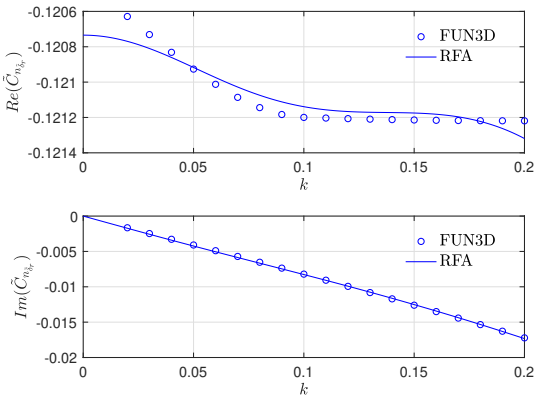

(c) $\tilde{C}_{n_{\tilde{\delta}_r}}$ vs. $\tilde{\delta}_r$

Figure 13. Frequency-Domain Regression of Linear Dynamic Control Derivatives of Side Force, Rolling Moment, and Yawing Moment Coefficients for Rudder

IV. Conclusions

This paper presents a nonlinear control derivative estimation method in the frequency domain. A high-order polynomial time-domain unsteady aerodynamic model is developed to accurately capture the unsteady aerodynamic forces and moments due to large control surface deflections. Using high-fidelity CFD simulations of control surface oscillations, time-domain aerodynamic force and moment coefficients are converted into the frequency domain using a Fourier series analysis. A frequency-domain regression is performed to extract the nonlinear dynamic control derivatives. Due to nonlinearity, the fundamental harmonic of the nonlinear terms contribute to the linear unsteady aerodynamic response in the frequency domain. A method is developed to separate the nonlinear contribution from the linear unsteady aerodynamic response.

The method is applied to the Transonic Truss-Braced Wing. A complete set of dynamic linear and nonlinear control derivatives for the elevator, aileron, and rudder is obtained. The results show high nonlinearity in the dynamic control derivatives for the elevator and aileron deflections up to 20°. The dynamic control derivatives for the rudder deflections up to 10° are generally linear. The odd-power nonlinear dynamic control derivatives are generally more significant than the even-power nonlinear dynamic control derivatives for all the aerodynamic force and moment coefficients except for the drag coefficient where the converse is true.

Acknowledgment

The authors wish to acknowledge NASA Advanced Air Transport Technology project for the funding support of this work. The authors also acknowledge Boeing Research and Technology and in particular Christopher Droney, Neal Harrison, Michael Beyar, Eric Dickey, and Anthony Sclafani, along with the NASA technical POC, Gregory Gatlin, for their research conducted under the NASA BAART contracts NNL10AA05B and NNL16AA04B. The research published in this paper is made possible by the technical data and wind tunnel test data furnished under these BAART contracts.

References

[1]Wang, F., and Chen, L., "Numerical Prediction of Stability Derivatives for Complex Configurations," Procedia Engineering 99 (2015) 1561-1575.

[2]Ghoreyshi M., Bergeron K., Lofthouse, A., and Cummings R., "CFD Calculation of Stability and Control Derivatives For Ram-Air Parachutes," AIAA Applied Aerodynamics Conference, AIAA-2016-1536, 2016.

[3]Murmann, S., "A Reduced-Frequency Approach for Calculating Dynamic Derivatives," AIAA Aerospace Sciences Meeting, AIAA-2005-0840, 2005.

[4]Nguyen, N. and Xiong, J., "CFD-Based Frequency Domain Method for Dynamic Stability Derivative Estimation with Application to Tran-

sonic Truss-Braced Wing," AIAA Aviation Forum, Applied Aerodynamics, AIAA-2022-3596, June 2022.

[5]Harrison, N. A., Hoffman, K., Lazzara, D. S., Reichenbach, E. Y., Sclafani, A. J., and Droney, C. K., "Subsonic Ultra Green Aircraft Research: Phase IV Final Report - Volume I Mach 0.80 Transonic Truss-Braced Wing High-Speed Design Report," NASA/CR-20220016017, October 2023.

[6]Theodorsen, T., "General Theory of Aerodynamic Instability and the mechanism of Flutter", NACA Report No. 496, 1949.

[7]Nguyen, N. and Xiong, J., "Frequency Domain Method for Dynamic Control Derivative Estimation with Application to Transonic Truss-Braced Wing," AIAA Applied Aerodynamics Conference, AIAA-2023-3945, June 2023.

[8]Harrison, N. A., Gatlin, G. M., Viken, S. A., Breyar, M., Dickey, E. D., Hoffman, K., and Reichenbach, E. Y., "Development of an Efficient M=0.80 Transonic Truss-Braced Wing Aircraft," AIAA-2020-0011, January 2020.

[9]Xiong, J. and Nguyen, N., "Steady and Unsteady Simulations of Transonic Truss-Braced Wing Aircraft for Flight Dynamic Stability Analysis," AIAA Applied Aerodynamics Conference, June 2022.